metals

MDPI

Article

An Efficient and Stable MXene-Immobilized, Cobalt-Based Catalyst for Hydrogen Evolution Reaction

Wei Guo, Buxiang Wang and Qing Shu *

School of Chemistry and Chemical Engineering, Jiangxi University of Science and Technology, Ganzhou 341000, China; gwzytj2021@163.com (W.G.)
* Correspondence: shuqing@jxust.edu.cn

Abstract: Hydrogen (H_2) is considered to be the best carbon-free energy carrier that can replace fossil fuels because of its high energy density and the advantages of not producing greenhouse gases and air pollutants. As a green and sustainable method for hydrogen production, the electrochemical hydrogen evolution reaction (HER) has received widespread attention. Currently, it is a great challenge to prepare economically stable electrocatalysts for the HER using non-precious metals. In this study, a $Co/Co_3O_4/Ti_3C_2T_x$ catalyst was synthesized by supporting Co/Co_3O_4 with $Ti_3C_2T_x$. The results show that $Co/Co_3O_4/Ti_3C_2T_x$ has excellent HER activity and durability in 1 mol L^{-1} KOH, and the overpotential and Tafel slope at 10 mA·cm^{-2} were 87 mV and 61.90 mV dec^{-1}, respectively. The excellent HER activity and stability of $Co/Co_3O_4/Ti_3C_2T_x$ can be explained as follows: $Ti_3C_2T_x$ provides a stable skeleton and a large number of attachment sites for Co/Co_3O_4, thus exposing more active sites; the unique two-dimensional structure of $Ti_3C_2T_x$ provides an efficient conductive network for rapid electron transfer between the electrolyte and the catalyst during electrocatalysis; Co_3O_4 makes the $Co/Co_3O_4/Ti_3C_2T_x$ catalyst more hydrophilic, which can accelerate the release rate of bubbles; Co/Co_3O_4 can accelerate the adsorption and deionization of H_2O to synthesize H_2. This study provides a new approach for the design and preparation of low-cost and high-performance HER catalysts.

Keywords: $Ti_3C_2T_x$; Co/Co_3O_4; electrocatalysis; hydrogen evolution reaction; alkaline media

check for updates

Citation: Guo, W.; Wang, B.; Shu, Q. An Efficient and Stable MXene-Immobilized, Cobalt-Based Catalyst for Hydrogen Evolution Reaction. *Metals* **2024**, *14*, 922. https://doi.org/10.3390/met14080922

Academic Editor: Yoshitsugu Kojima

Received: 3 July 2024
Revised: 6 August 2024
Accepted: 12 August 2024
Published: 14 August 2024

Copyright: © 2024 by the authors. Licensee MDPI, Basel, Switzerland. This article is an open access article distributed under the terms and conditions of the Creative Commons Attribution (CC BY) license (https://creativecommons.org/licenses/by/4.0/).

1. Introduction

In order to deal with the energy crisis and environmental protection issues, countries around the world have been increasing their attention to new clean energy. Among many kinds of new clean energy sources available on the globe, hydrogen (H_2) is considered to be the best carbon-free energy carrier that can replace fossil fuels. In the current hydrogen production technology, the electrochemical decomposition of water to produce hydrogen is considered to be one of the best and the most efficient and greenest hydrogen production methods [1–3]. An electrochemical water decomposition reaction is composed of the oxygen evolution reaction (OER) and hydrogen evolution reaction (HER), in which the HER is the key step. A catalyst that can reduce the reaction barrier and energy consumption, increase the reaction efficiency and improve the reaction rate plays a very important role in HER process. Therefore, the study of efficient electrocatalysts has become the most important part of HER technology exploration.

Numerous studies have found that precious metals such as platinum (Pt), ruthenium (Ru), palladium (Pd), gold (Au) and iridium (Ir) have more suitable ΔG_{H^*} values than other metallic elements. This may be due to the fact that precious metals have a surface defect, which makes the active substance easily adsorbed on their surface and facilitates the formation of active intermediates [4]. Pt-based material is currently recognized as the best HER electrocatalyst, and its ΔG_{H^*} value is almost zero. However, the limited reserves and high price of Pt limit its large-scale application, and therefore, it is not suitable for

commercial hydrogen production [5]. Therefore, it is urgent to develop high-efficiency and low-cost HER electrocatalysts.

At present, a large number of studies have found that transition metals (such as Fe, Co, Ni, etc.) and transition metal oxides show high electrocatalytic activity for HER in alkaline solutions and are attractive candidates for HER electrocatalyst. Compared with the small global reserves and high market prices of precious metals, transition metals have abundant global reserves and cost advantages. The ΔG_{H^*} value of Co is moderate, and Co-based materials such as cobalt phosphide, cobalt selenide, cobalt sulfide and cobalt layered double hydroxides (Co-LDHs) have diversified characteristics in terms of their composition, crystal structure and reversible morphology. Results show that Co-based materials have great potential for the HER. However, despite the advantages of Co-based materials in terms of HER catalytic activity, there are still some shortcomings in their industrial applications. For example, cobalt oxide can dissolve in acidic solutions, resulting in the loss of active sites; agglomeration often occurs during the preparation of cobalt selenide; low conductivity can reduce the HER activity of cobalt sulfide, cobalt phosphide and Co-LDHs [6]. In order to realize the practical application of cobalt-based materials in the HER, some researchers have tried various strategies, such as constructing nanostructures, carbon material loading, morphological control and doping. For example, Wang et al. synthesized Co@CoO nanowires and found that they are excellent catalysts for hydrogen production at low overpotential [7]. He et al. improved the HER efficiency of Co-Ni phosphide (Co-Ni-P) in an alkaline solution by anchoring hollow Co-Ni-P nanospheres on reduced graphene oxide nanosheets (RGO) [8]. Gao et al. synthesized a nuclear/shell structure Co_3O_4@CoS_2 nanoarray with excellent HER activity in acidic solutions [9]. Zhang et al. synthesized a highly efficient HER electrocatalyst, Ni_2P/CoP@C-NSG, suitable for acidic solutions by loading highly dispersed Ni_2P and CoP onto carbon nanospheres and growing Ni_2P/CoP on a N and S co-doped graphene substrate [10]. In general, transition metal oxides are good for the dissociation of water but bad for the recombination of adsorbed hydrogen atoms (H_{ad}) to form H_2. However, transition metals can effectively adsorb hydrogen atoms and promote the conversion of H_{ad} to H_2. Therefore, researchers have set out to construct transition metal/metal oxide catalysts suitable for the HER. For example, Wang et al. reported a cobalt-based electrocatalyst, Co/CoO/$CoMoO_3$, with a highly dispersed metal/metal oxide active component and a tight series structure that together promoted the efficient conduct of the HER under a high current density in a medium/alkaline electrolyte. Through experiments and DFT calculations, it was found that the strong OH adsorption at CoO site promotes the dissociation of water, and the appropriate H adsorption at Co sites promotes the precipitation of hydrogen, thus achieving the high current density of the HER in alkaline and neutral media [11].

In recent years, a large number of studies have found that the introduction of suitable substrates to disperse and anchor Co-based catalytic species is a feasible way to improve its utilization efficiency, because it can expose as many active points on the catalyst surface as possible [12–15]. Therefore, the HER performance of Co-based materials can be improved by selecting a suitable carrier [16]. MXene ($Ti_3C_2T_x$) is the general term for a series of novel two-dimensional (2D) transition metal carbide and carbon nitride materials with graphene-like structures. Compared to traditional three-dimensional (3D) catalysts, $Ti_3C_2T_x$ has a larger surface area and can provide a large number of attachment points for active substances. At the same time, the good electrical conductivity of $Ti_3C_2T_x$ can accelerate the transfer of electrons from the electrode to the catalyst surface. Therefore, it may be a suitable carrier for loading cobalt-based active components. However, due to the influence of van der Waals forces, $Ti_3C_2T_x$ nanosheets are easy to accumulate or stack, which easily leads to the catalytic active site being covered up. It is worth noting that the layer spacing of MXene obtained via HF etching of the MAX phase can be expanded. The large layer spacing facilitates the entry of active substances into the interior of $Ti_3C_2T_x$, and the loaded active components can play a role in supporting the structure to prevent the stacking of $Ti_3C_2T_x$. Therefore, this study attempted to use $Ti_3C_2T_x$ loaded with Co-based active components.

Through the above attempts, the HER activity of the Co-based active component can be improved by dispersing and anchoring $Ti_3C_2T_x$. On the other hand, the stacking of $Ti_3C_2T_x$ can be prevented by Co-based active components. Therefore, it is expected that the electrocatalyst with high HER activity can be prepared through the synergistic action of the carrier and cobalt-based catalyst.

Metal-supported electrocatalysts are generally prepared via the high-temperature H_2 reduction of metal. However, due to the hightemperature, the H_2 reduction method has the characteristics of a strong heating effect, and it may accelerate the growth of particles on the catalyst surface and the agglomeration of metal active centers, resulting in the reduction of metal dispersion and specific surface area of the catalyst, which has a negative impact on the catalytic performance. In order to reduce the agglomeration of metal active centers during the reduction process, using $NaBH_4$ as a reducing agent is an effective strategy for preparing metal-supported electrocatalysts. Compared with the H_2 reduction method, the $NaBH_4$ reduction process is carried out in a solution at room temperature so that the solvent can disperse the reactants and quickly absorb the heat generated by the exothermic reaction, thus slowing down the agglomeration of metal active centers in the reduction process.

However, the synthesis of catalysts suitable for the HER by supporting cobalt-based active components with $Ti_3C_2T_x$ is rarely reported. Therefore, in this study, $Ti_3C_2T_x$ was prepared using ultrasonic-assisted HF etching of Ti_3AlC_2 and then used as the carrier to support the Co-based active component (Co/Co_3O_4). Subsequently, the $Co/Co_3O_4/Ti_3C_2T_x$ catalyst was prepared through the liquid-phase reduction method using $NaBH_4$ as the reducing agent. The structure, morphology, crystal phase and elemental valence of the obtained catalyst were analyzed using various characterization methods. The activity and stability of $Co/Co_3O_4/Ti_3C_2T_x$ during electrocatalysis of the HER were studied in electrolytes of 1 mol L^{-1} KOH and 0.5 mol L^{-1} H_2SO_4.

2. Materials and Methods

2.1. Reagents

The reagents used are as follows: $Co(NO_3)_2{\cdot}6H_2O$ (analytical grade, Sinopharm Chemical Reagent Co., Ltd., Shanghai, China), $NaBH_4$ (analytical grade, Sinopharm Chemical Reagent Co., Ltd., Shanghai, China), Ti_3AlC_2 (analytical grade, Zhejiang Yamei Nano Technology Co., Ltd., Jiaxing, China) and HF (analytical grade, Shanghai Aladdin Technology Co., Ltd., Shanghai, China).

2.2. Synthesis of $Co/Co_3O_4/Ti_3C_2T_x$ Catalyst

$Ti_3C_2T_x$ preparation was performed as follows: First, 20 mL of 48% aqueous HF solution was transferred to a Teflon beaker with a volume of 200 mL. Subsequently, 1.00 g of Ti_3AlC_2 powder was slowly added to the above-mentioned beaker within 30 min and electromagnetically stirred for 24 h at 150 rpm and 55 °C. The resulting solution was centrifuged at 6400 rpm for 10 min to yield the sediment and recycle the supernatant (including the HF solution and etched Al layers), respectively. The obtained sediment was cleaned with deionized water several times until the pH of the dispersion was close to 6. Finally, the resulting powder ($Ti_3C_2T_x$) was dried in a vacuum oven at 60 °C for 24 h. The dried powder was obtained and identified as $Ti_3C_2T_x$ (T_x stands for O, F and OH functional groups).

The $Co/Co_3O_4/Ti_3C_2T_x$ catalyst preparation occurred as follows: First, 0.30 g $Ti_3C_2T_x$ was added to a beaker containing 25 mL of deionized water and treated with an ultrasonic device in an ice water bath for 2 to 3 h. Subsequently, the $Ti_3C_2T_x$ solution was obtained after the above-mentioned solution was clearly stratified; second, 0.8 g of $Co(NO_3)_2{\cdot}6H_2O$ was added to the $Ti_3C_2T_x$ solution and electromagnetically stirred for 30 min at 800 rpm and 25 °C. After standing for 3 h, the solution became clear and stratified to obtain a $Co/Co_3O_4/Ti_3C_2T_x$ solution; third, some $NaBH_4$ was added until the solution was clear and layered (the upper layer was colorless and transparent), magnetically stirred at 800 rpm for 30 min and left for 12 h. The white liquid in the beaker was poured away, and the

remaining sediment was dried in the freeze dryer for 48 h to obtain $Co/Co_3O_4/Ti_3C_2T_x$. The preparation process of $Co/Co_3O_4/Ti_3C_2T_x$ is shown in Figure 1.

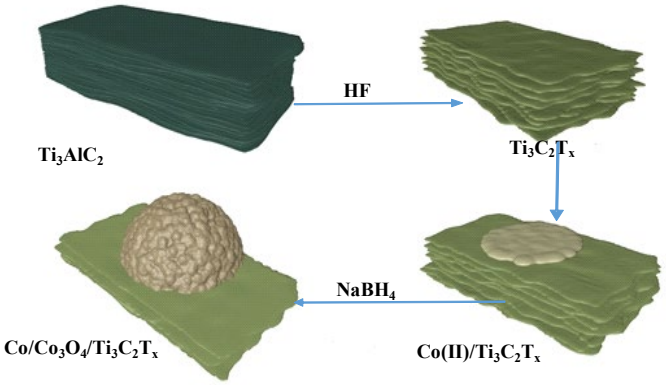


Figure 1. Schematic diagram of $Co/Co_3O_4/Ti_3C_2T_x$ preparation.

2.3. Catalyst Characterization

The functional groups of $Ti_3C_2T_x$ were identified using Fourier infrared spectroscopy (FT-IR) (Nicolet 5700, Madison, WI, USA). The crystalline phases of the obtained catalyst were analyzed using X-ray diffraction (XRD) (PANalytical, Empyean, Almelo, The Netherlands) with Cu Kα radiation (λ = 0.15418 nm) at 40 kV and 40 mA over a 2θ range from 5° and 85°, and the XRD results of the samples were compared with existing standard cards to determine their phase structure. The surface morphologies and chemical compositions of the catalysts were investigated using a scanning electron microscope (SEM) (MLA650F, FEI Company, Hillsboro, OR, USA) equipped with an energy-dispersive X-ray spectroscope (EDS, Quantax 400, Bruker, Ettlingen, Germany) at an accelerating voltage of 20 kV. The size, shape and distribution of the obtained catalyst were analyzed using a transmission electron microscope (TEM) (TecnaiG2-20, FEI Company, Hillsboro, OR, USA). The chemical valence states of the elements in the catalyst were measured using X-ray photoelectron spectroscopy (XPS) (Escalab Xi+, Thermo Fisher Scientific Inc., Oxford, UK) under the vacuum condition of 8×10^{-10} Pa. A monochromatic Al Kα X-ray source (hv = 1486.6 eV) was used with a working voltage of 12 kV. The specific surface area and pore size distribution of the catalyst were measured using a N_2 physical adsorption instrument (ASAP 2020, Micromeritics Instrument Ltd., Norcross, GA, USA) at 77 K. The contact angle of the catalyst was measured using a contact angle measuring instrument (JY-Pha, Chengde Yote Instrument Manufacturing Co. Ltd., Chengde, China) to determine the surface wettability.

2.4. Electrocatalytic Hydrogen Evolution Test of Catalyst

For the preparation of test electrode, first, 1 mg of the catalyst was weighed and ground to powder; second, it was dispersed in a solution composed of 0.25 mL of isopropyl alcohol, 0.75 mL of deionized water and 20 μL of 5 wt% Nafion solution; third, the suspension was dispersed via ultrasonic treatment under the condition of an ice-water bath until 1 mL of uniformly dispersed suspension was formed. Finally, the solution containing the catalyst was coated on the surface of the carbon paper with an area of 1 cm^2, and the working electrode supported by the catalyst was obtained after completely drying.

The HER performance of the catalyst was tested on a CHI660E electrochemical workstation at 25 °C. A standard three-electrode system was adopted, with a spectral pure graphite rod as the auxiliary electrode and a saturated calomel electrode (SCE) as the reference electrode. The potentials are all relative to the reversible hydrogen electrode (RHE). The conversion formula is shown in Equation (1):

$$V_{(RHE)} = V_{(SCE)} + 0.0591 \times pH + 0.2415 \quad (1)$$

where $V_{(RHE)}$ is the potential value (V) of the RHE, $V_{(SCE)}$ is the potential value (V) of the SCE, and pH is the pH value of the solution.

In this study, the non-Faraday, dual-layer capacitance currents corresponding to the cyclic voltammetry curve (CV) of the catalyst under different scanning rates (10, 20, 30, 40, 50, 60, 70, 80, 90 and 100 mV s^{-1}) were tested. After linear fitting, the cyclic voltammetry curves were developed. The capacitance of the electrochemical double-layer capacitance (C_{dl}) was calculated using Equation (2):

$$I = V \times C_{dl} \quad (2)$$

where V is the scanning rate (mV s^{-1}), and I is the current density at different scanning rates (mA cm^{-2}).

In order to evaluate the true electrocatalytic activity of the catalyst, the electrochemically active surface area (ECSA, cm^{-2}) involved in the electrochemical catalytic reaction should be calculated. The ECSA value can be calculated from the C_{dl} value using the Randles–Sevcik equation, as shown in Equation (3):

$$ECSA = \frac{C_{dl}}{C_s} \quad (3)$$

where the C_s value is the specific capacitance (mF) of the corresponding surface smooth sample under the same conditions. The C_s value is usually in the range of 20–60 mF [17], and the C_s value was set as 40 mF in this study.

In general, the electrocatalytic activities of different catalysts can be compared by their overpotential (η) values at a current density of 10 mA cm^{-2}. η values can be calculated using the linear sweep voltammetry (LSV) curve derived from the linear sweep voltammetry (LSV) method, which is usually applied to the electrode with a continuously linear voltage (−0.6 V vs. RHE), and the resulting current is monitored. Since this type of current depends on the rate of oxidation or reduction occurring at the electrode, the size of the current in the LSV curve can reflect the degree of HER. In this study, the scanning rate was set at 5 mV s^{-1} for LSV testing. Then, a line at $y = -10$ was made, and the abscissa of the intersection point of the LSV curve was the η value after taking the absolute value.

The Tafel slope (b) is the rate at which the current increases with respect to η, which is mainly determined by the transfer coefficient. The smaller the b value is, the faster the current density increases and the smaller the η change, indicating that the rate-determining step is at the end of the multi-electron transfer reaction, which usually marks an electrocatalyst with excellent performance. The current density and potential data of the LSV diagram are converted into a graph of log(current density i) and η values; that is, the Tafel diagram is obtained. Then, the linear fitting was carried out through Origin 8 software, and the b value was calculated using Equation (4):

$$\eta = b \log I + a \quad (4)$$

where η is the overpotential (mV), I is the current density (mA cm^{-2}), a is the constant, and b is the Tafel slope.

The larger the surface area of the catalyst, the more active sites are exposed to the electrocatalyst surface, and the mass activity (MA) value is more indicative of the true activity of the catalyst. In general, a smaller-sized catalyst has higher MA value because a smaller-sized particle means that the ratio of surface atoms to total atoms is larger, exposing more electrocatalytic active sites. In order to more intuitively compare the activities of different catalysts, the MA values can be calculated according to Equation (5):

$$MA = I/M \quad (5)$$

where MA (mA mg^{-1}) is the mass activity of the catalyst, I is the current density (mA cm^{-2}), and M is the catalyst load (mg cm^{-2}).

The stability of the catalyst was tested using a chronocurrent method (i − t), which is usually performed at a constant potential and monitors changes in the electrode current. In addition, the stability of the electrocatalyst was tested using the CV method with more than 1000 cycles, which was achieved by comparing the LSV data before and after the stability test. All CV, LSV, i − t and other tests were performed in electrolytes of 1 mol L^{-1} KOH or 0.5 mol L^{-1} H_2SO_4, and the obtained data were not corrected by IR compensation.

3. Results

3.1. Characterization of Catalyst

The FT-IR result of the $Ti_3C_2T_x$ is shown in Figure 2. There are three characteristic peaks of $Ti_3C_2T_x$ in Figure 2, corresponding to C=O stretching vibrations, O-H bending vibrations and O-H stretching vibrations at 1633, 1393 and 3446 cm^{-1}, respectively.

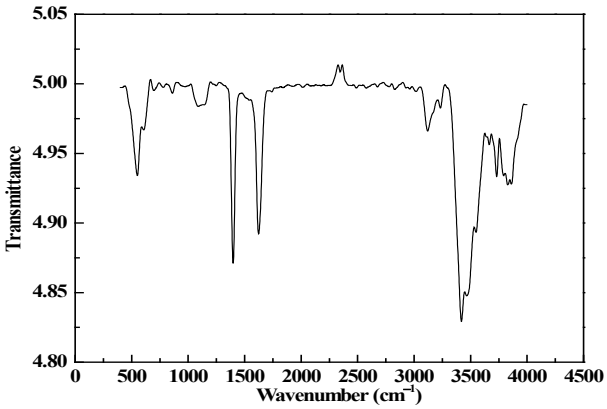


Figure 2. FT-IR spectrum of Ti_3C_2.

The surface morphologies of $Ti_3C_2T_x$ and $Co/Co_3O_4/Ti_3C_2T_x$ were characterized using an SEM, and the results are shown in Figure 3. It can be observed from Figure 3a that the $Ti_3C_2T_x$ obtained via HF etching Ti_3AlC_2 has an obvious "organ-like" morphology, which is conducive to the active substance to penetrate the internal structure of Ti_3AlC_2. The morphology is formed due to the destruction of Ti-Al bonds between the etched layers, which is consistent with other researchers' reports [18]. It can be clearly observed from Figure 3b that the surface of the obtained $Co/Co_3O_4/Ti_3C_2T_x$ has particle clusters with different sizes and shapes. The formation of these particles can be attributed as follows: during the reduction reaction, a large amount of Co^{2+} is reduced by $NaBH_4$ to zero-valent Co, which accumulates and deposits on the surface of $Ti_3C_2T_x$ [19].

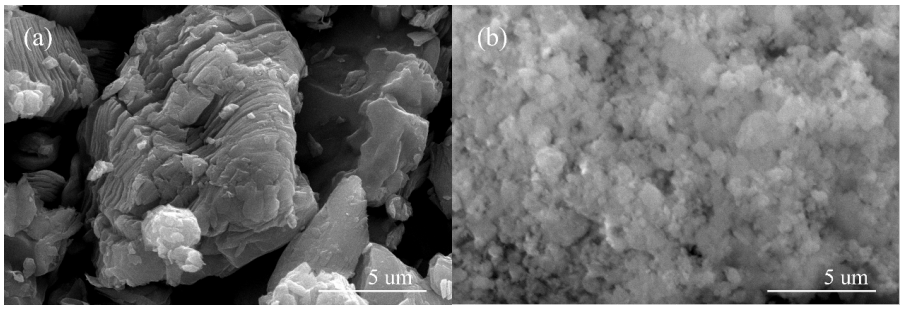


Figure 3. SEM images of $Ti_3C_2T_x$ and $Co/Co_3O_4/Ti_3C_2T_x$. (**a**) $Ti_3C_2T_x$; (**b**) $Co/Co_3O_4/Ti_3C_2T_x$.

In order to understand the types and distribution of elements in the catalyst, the $Co/Co_3O_4/Ti_3C_2T_x$ catalyst shown in Figure 4a was analyzed using element surface scanning, and the results are shown in Figure 4b–f.

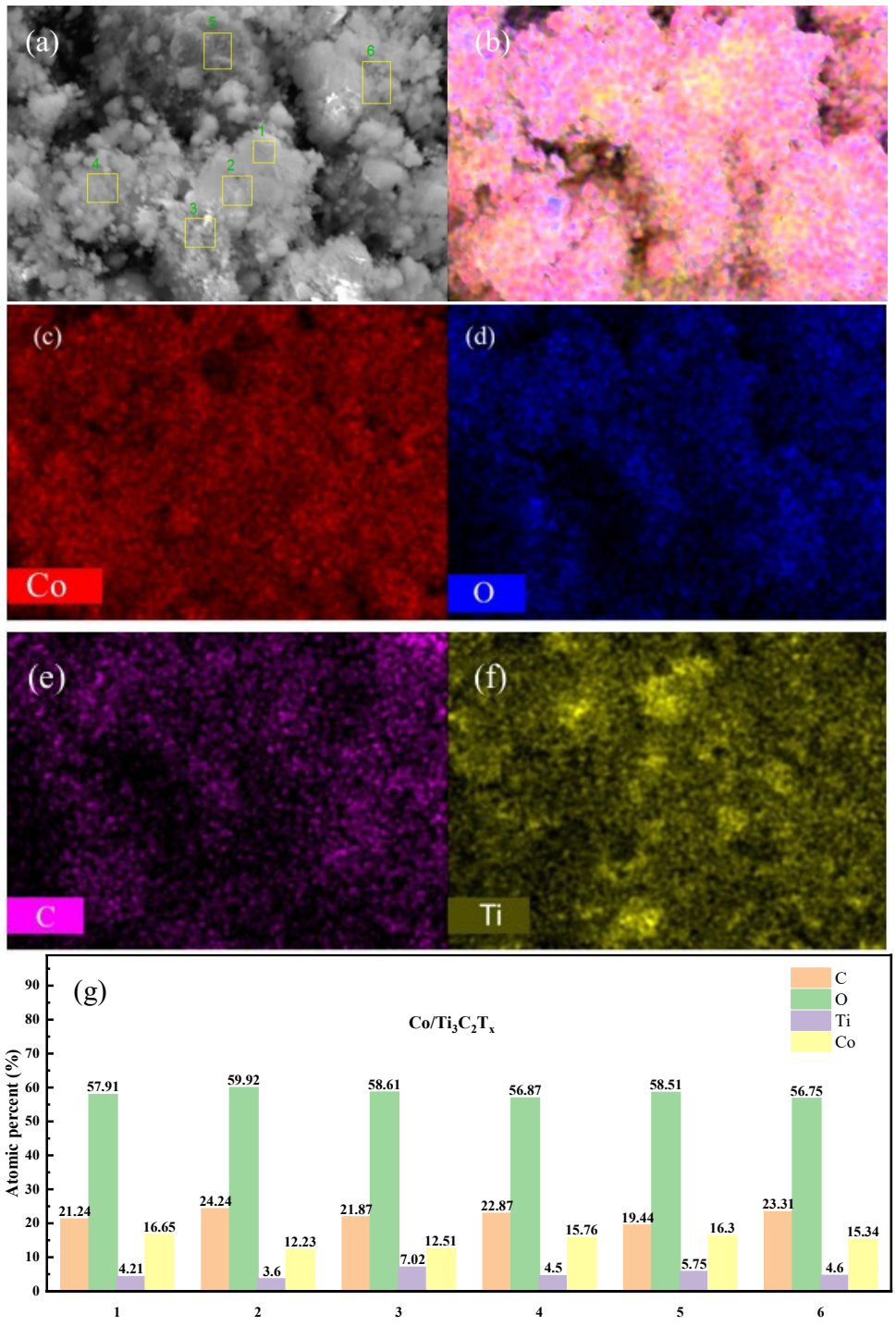


Figure 4. Elemental analysis diagram of $Co/Co_3O_4/Ti_3C_2T_x$. (**a**) SEM diagram of $Co/Co_3O_4/Ti_3C_2T_x$; (**b**) EDS mapping of $Co/Co_3O_4/Ti_3C_2T_x$ and (**c**) Co element, (**d**) O element, (**e**) C element and (**f**) Ti element; (**g**) atomic ratios of Co, O, C and Ti elements.

Many bright and evenly distributed areas can be seen in Figure 4b, indicating that the elements Co and O are evenly distributed on the surface of $Ti_3C_2T_x$, which helps expose more active sites on the catalyst surface. Then, six square regions were randomly selected on the surface of $Co/Co_3O_4/Ti_3C_2T_x$, and the element information of each square region was detected. The results are shown in Figure 4g. It can be seen from Figure 4g that the atomic proportion of the same element at each detection point is close, which further indicated that the distribution of the elements Co and O is relatively uniform. The average

atomic contents of C, O, Ti and Co are 22.16%, 58.10%, 4.95% and 14.80%, respectively. The high O content in $Co/Co_3O_4/Ti_3C_2T_x$ indicates the presence of cobalt oxide.

In order to further explore the structural information of catalysts, the morphologies of $Ti_3C_2T_x$ and $Co/Co_3O_4/Ti_3C_2T_x$ were observed using a TEM, and the results are shown in Figure 5. It can be seen from Figure 5a that $Ti_3C_2T_x$ presents a unique two-dimensional sheet structure with many active edge sites, which can provide a large number of attachment sites for the loaded active substances. As shown in Figure 5b, a large number of clusters are attached to the surface of the layered $Co/Co_3O_4/Ti_3C_2T_x$. This may be because $NaBH_4$ reduced a large amount of Co^{2+} to Co, and then, Co particles gathered and deposited on the surface of $Ti_3C_2T_x$ [20], which was consistent with the results of the SEM analysis.

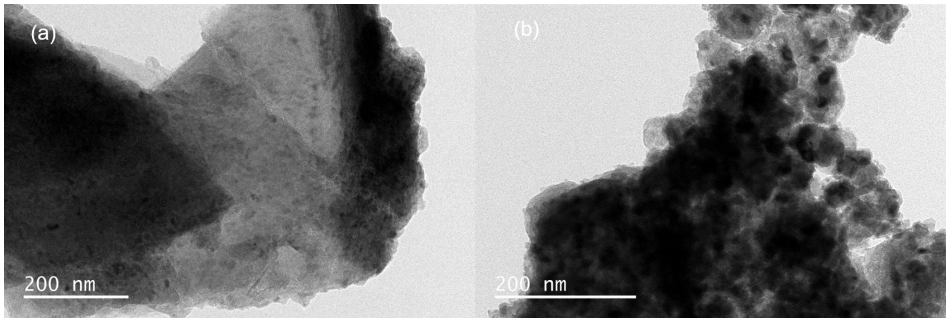


Figure 5. TEM images of (**a**) $Ti_3C_2T_x$ and (**b**) $Co/Co_3O_4/Ti_3C_2T_x$.

The crystal structures and compositions of Ti_3AlC_2, $Ti_3C_2T_x$ and $Co/Co_3O_4/Ti_3C_2T_x$ were obtained using XRD. It can be seen from the XRD patterns of Ti_3AlC_2 and $Ti_3C_2T_x$ shown in Figure 6a that after HF etching of Ti_3AlC_2, obvious characteristic diffraction peaks appeared at 2θ of 9.5°, 19.3° and 39.0°. By comparing the standard card of Ti_3AlC_2 (JCPDS NO.52-0875), it can be inferred that the above characteristic diffraction peaks correspond to the (002), (004) and (104) crystal faces, respectively. The characteristic diffraction peak (104) of Al in the MAX structure almost completely disappeared, indicating that the Al layer had been completely etched. In addition, Ti_3AlC_2 shows a new wide characteristic diffraction peak at 2θ of 6.1°, indicating that the (002) characteristic diffraction peak corresponding to MXene moved from 9.5° to a lower angle of 6.1°. According to the Bragg equation, the layer spacing of MXene obtained by etching the MAX phase was enlarged. The larger layer spacing facilitates the active substances to enter the interior of $Ti_3C_2T_x$, and the active components can support the structure and prevent the stacking of $Ti_3C_2T_x$ [20,21]. The XRD pattern of $Co/Co_3O_4/Ti_3C_2T_x$ is shown in Figure 6b. Four characteristic diffraction peaks appeared at 2θ of 41.6°, 44.6°, 47.4° and 75.5°, respectively. By comparing the standard card of Co (JCPDS NO.05-0727), it can be inferred that the above characteristic diffraction peaks correspond to the (100), (002), (101) and (110) crystal faces, respectively. At the same time, six characteristic diffraction peaks appeared at 2θ of 34.1°, 39.6°, 57.3°, 68.4, 71.9 and 85.4°, respectively. By comparing the standard card of CoO (JCPDS NO. 42-1300), it can be inferred that the above characteristic diffraction peaks correspond to the (111), (200), (220), (311), (222) and (400) crystal faces. In addition, the XRD pattern of $Co/Co_3O_4/Ti_3C_2T_x$ shows that there are seven characteristic diffraction peaks at 2θ of 19.0°, 31.3°, 36.7°, 38.5°, 44.8°, 59.3° and 65.3°. Compared with the standard card of Co_3O_4 (JCPDS NO.43-1003), it can be inferred that the above characteristic peaks correspond to the crystal faces of (111), (220), (311), (222), (400), (511) and (440), respectively. This also proves that the Co element in $Co/Co_3O_4/Ti_3C_2T_x$ exists in metallic and oxidized states (Co, CoO and Co_3O_4). In addition, $Co/Co_3O_4/Ti_3C_2T_x$ showed eleven characteristic diffraction peaks corresponding to MXenes at 2θ of 9.5°, 19.0°, 33.9°, 36.6°, 39.1°, 41.6°, 48.3°, 56.7°, 60.0°, 65.3°, 70.2° and 73.9°, respectively. In summary, the $Co/Co_3O_4/Ti_3C_2T_x$ catalyst was successfully prepared.

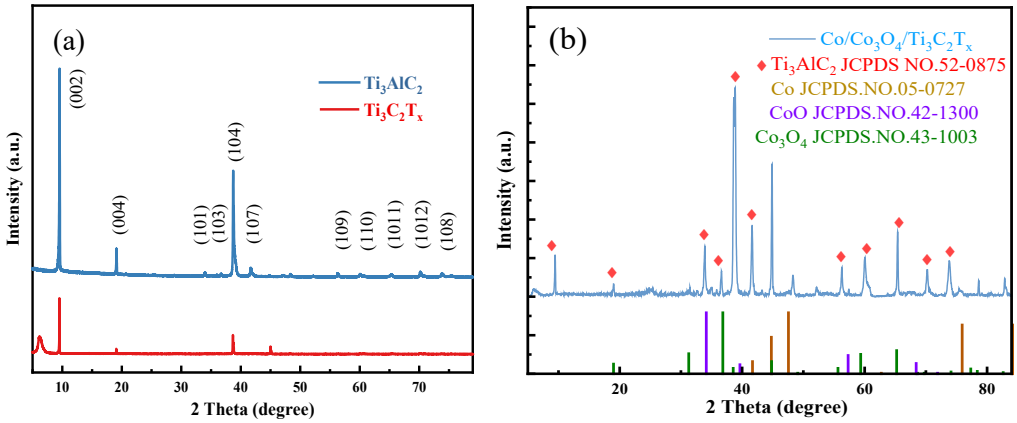


Figure 6. XRD patterns of Ti_3AlC_2, $Ti_3C_2T_x$ and $Co/Co_3O_4/Ti_3C_2T_x$. (**a**) Ti_3AlC_2 and $Ti_3C_2T_x$; (**b**) $Co/Co_3O_4/Ti_3C_2T_x$.

The elemental composition of the $Co/Co_3O_4/Ti_3C_2T_x$ catalyst was analyzed using XPS. Figure 7a shows the full XPS spectrum of $Co/Co_3O_4/Ti_3C_2T_x$, and binding energy peaks corresponding to Co, O, Ti, C and other elements can be clearly seen in the full spectrum. Furthermore, the fine spectrum of C1s was obtained via narrow-area scanning (Figure 7b), which can be divided into three peaks with binding energies of 284.8 eV, 286.4 eV and 289.0 eV, corresponding to C-C, O-C and O-C=O, respectively [22,23]. Figure 7c shows the fine spectrum of Co2p, which can be divided into three peaks with binding energies of 780.1 eV, 781.1 eV and 782.7 eV, respectively, attributed to Co^0, Co^{3+} and Co^{2+} [24], indicating that Co exists in the form of metallic Co and in the oxidation state as Co_3O_4, which is consistent with the XRD analysis results. It is worth noting that most of the Co2p peaks are Co^{2+}. Figure 7d shows the fine spectrum of O1s, which can be divided into three characteristic peaks with binding energies of 530.7 eV, 531.2 eV and 532.2 eV, respectively, attributed to Co-O, −OH and O in the adsorbed H_2O [25], which means that O in the catalyst exists in two forms: lattice oxygen and surface hydroxyl oxygen. The surface of the catalyst contains both cobalt oxide (Co-O) and cobalt hydroxide (Co-OH), which can effectively accelerate the dissociation of water [26,27]. In addition, the appearance of the binding energy peak corresponding to oxygen in the adsorbed H_2O also indicates that the catalyst has a certain hydrophilicity.

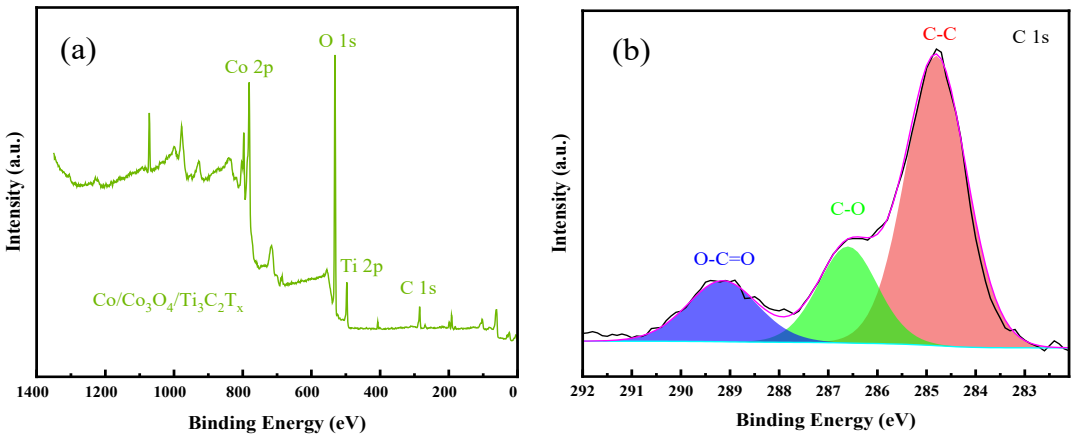


Figure 7. *Cont.*

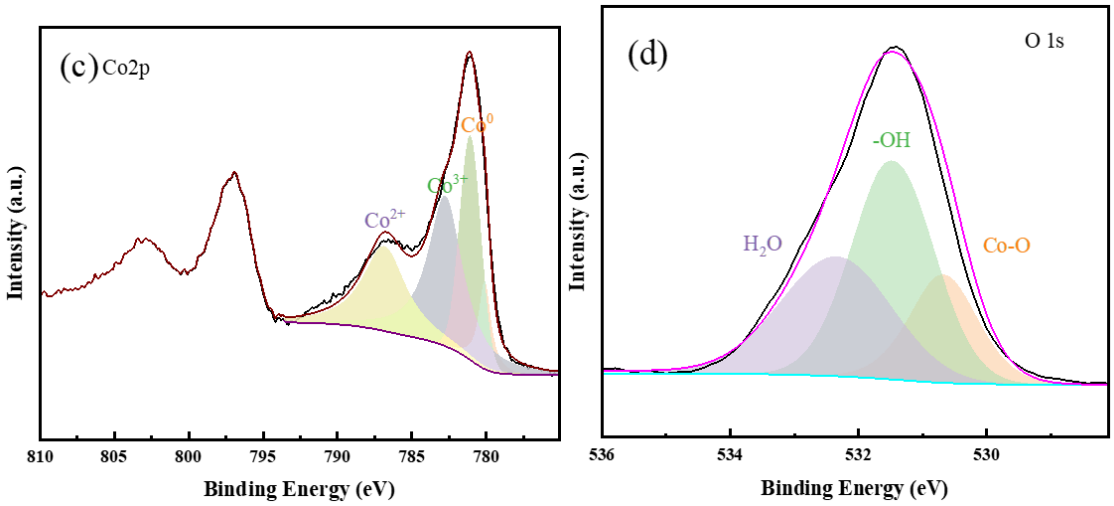


Figure 7. XPS diagram of $Co/Co_3O_4/Ti_3C_2T_x$. (**a**) XPS full spectrum, (**b**) C1s spectrum, (**c**) Co2p spectrum and (**d**) O1s spectrum.

The hydrophilicity of the catalyst has a great influence on the HER. Hence, the hydrophilicity of the catalyst was detected by measuring the contact angles of $Ti_3C_2T_x$, Co and $Co/Co_3O_4/Ti_3C_2T_x$, and the results are shown in Figure 8a–c. As can be seen from Figure 8a–c that the contact angles of $Ti_3C_2T_x$, Co and $Co/Co_3O_4/Ti_3C_2T_x$ are 141.9°, 122.1° and 11.7°, respectively. The contact angle of $Co/Co_3O_4/Ti_3C_2T_x$ is much smaller than those of $Ti_3C_2T_x$ and Co, which indicates that the hydrophilicity of $Co/Co_3O_4/Ti_3C_2T_x$ is much stronger than those of $Ti_3C_2T_x$ and Co. The possible reasons are as follows: a portion of Co on the surface of $Co/Co_3O_4/Ti_3C_2T_x$ is oxidized to Co_3O_4, which endows the catalyst to have a higher degree of hydrophilicity. When the HER occurs, the stronger the hydrophobicity of the catalyst surface, the shorter the retention time of the generated bubbles on the catalyst surface and the smaller the bubble size when leaving the surface, which means that the reaction speed of the HER is faster [28].

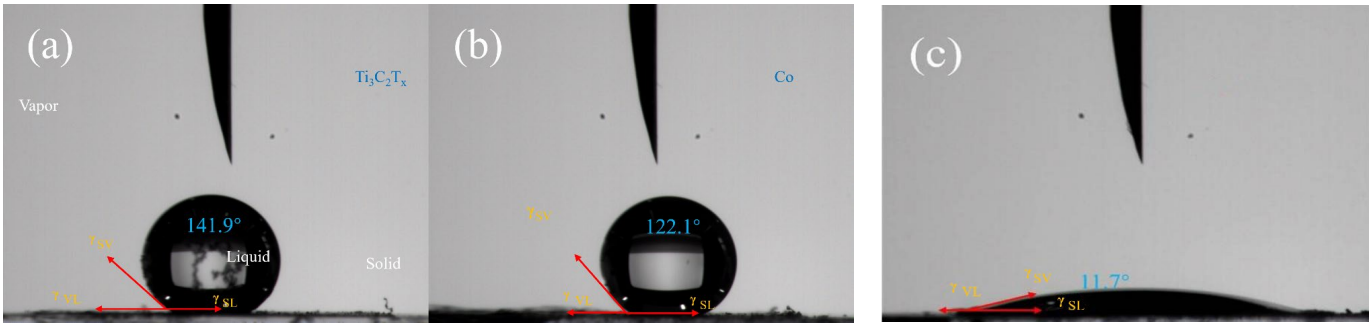


Figure 8. Contact angles of $Ti_3C_2T_x$, Co and $Co/Co_3O_4/Ti_3C_2T_x$. (**a**) $Ti_3C_2T_x$, (**b**) Co and (**c**) $Co/Co_3O_4/Ti_3C_2T_x$.

The specific surface area and aperture of $Ti_3C_2T_x$, Co and $Co/Co_3O_4/Ti_3C_2T_x$ were measured using the specific surface area tester. Figure 9a shows the N_2 adsorption–desorption curve, in which the N_2 adsorption–desorption isothermal curve of $Co/Co_3O_4/Ti_3C_2T_x$ is type IV, indicating that there was a H3 hysteresis loop at a relative pressure p/p^0 of 0.45–0.9 caused by the capillary condensation of adsorbate. Therefore, the $Co/Co_3O_4/Ti_3C_2T_x$ had a mesoporous structure, and the pore structure was irregular. The pore diameters and specific surface areas of the catalysts are listed in Table 1. The specific surface area, pore volume and pore size of $Ti_3C_2T_x$ were 2.94 $m^2\ g^{-1}$, 0.0076 $cm^3\ g^{-1}$ and 10.71 nm. For comparison, the specific surface area of Co was 64.02 $m^2\ g^{-1}$, the pore volume was 0.30 $cm^3\ g^{-1}$, and the pore size was 186.79 nm. When $Ti_3C_2T_x$ was loaded

with Co/Co_3O_4, the specific surface area of $Co/Co_3O_4/Ti_3C_2T_x$ became 17.64 m^2 g^{-1}, and the pore volume was 0.04 cm^3 g^{-1}; both of them were increased. The pore size of $Co/Co_3O_4/Ti_3C_2T_x$ was 10.07 nm, which was similar to the pore size of $Ti_3C_2T_x$. It is worth noting that compared with $Ti_3C_2T_x$, the specific surface area, pore volume and pore diameter of $Co/Co_3O_4/Ti_3C_2T_x$ are greatly increased, which may be due to Co/Co_3O_4 infiltrating the interior of $Ti_3C_2T_x$ and effectively inhibiting the accumulation of $Ti_3C_2T_x$ flakes. This helps widen the layer spacing of the catalyst, thereby increasing the contact area between the catalyst and electrolyte, providing more active sites for the HER. In addition, the pore size distributions of $Ti_3C_2T_x$, Co and $Co/Co_3O_4/Ti_3C_2T_x$ are shown in Figure 9b. Compared with $Ti_3C_2T_x$ and $Co/Co_3O_4/Ti_3C_2T_x$, the pore size distribution of Co is wider, and the mesoporous distributions of Co and $Co/Co_3O_4/Ti_3C_2T_x$ were mainly in the range of 35–40 nm and 5–20 nm, respectively.

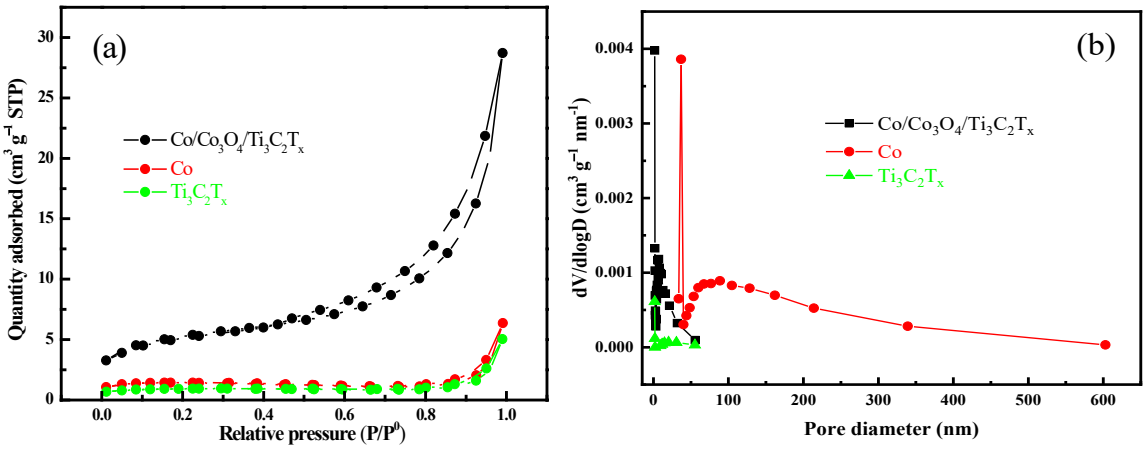


Figure 9. N_2 adsorption–desorption curves and pore size distributions of $Ti_3C_2T_x$, Co and $Co/Co_3O_4/Ti_3C_2T_x$. (**a**) N_2 adsorption–desorption curve; (**b**) pore size distribution (0–600 nm).

Table 1. Specific surface areas (BET), pore volumes (single-point method) and average pore diameters of $Ti_3C_2T_x$, Co and $Co/Co_3O_4/Ti_3C_2T_x$.

Catalyst	Specific Surface Area (m^2/g)	Pore Volume (cm^3/g)	Average Pore Diameter (nm)
$Ti_3C_2T_x$	2.94	0.0076	10.71
Co	64.02	0.30	186.79
$Co/Co_3O_4/Ti_3C_2T_x$	17.64	0.044	10.07

3.2. Electrocatalytic HER Performance Test in Acidic Electrolyte

The HER electrocatalytic activities of $Ti_3C_2T_x$, Co and $Co/Co_3O_4/Ti_3C_2T_x$ were tested in a 0.5 mol L^{-1} H_2SO_4 solution, and the LSV results are shown in Figure 10a. It can be seen from Figure 9a that the electrocatalytic activities of $Ti_3C_2T_x$ and Co are very low. However, when $Ti_3C_2T_x$ and Co formed $Co/Co_3O_4/Ti_3C_2T_x$, the electrocatalytic performance was significantly improved. Furthermore, the η values corresponding to $Ti_3C_2T_x$, Co and $Co/Co_3O_4/Ti_3C_2T_x$ at a current density of 10 mA cm^{-2} were obtained, and they were 599 mV, 517 mV and 86 mV. However, after only four LSV tests, the η value of $Co/Co_3O_4/Ti_3C_2T_x$ was changed from an initial 86 mV to 225 mV (see Figure 10b). The results show that $Co/Co_3O_4/Ti_3C_2T_x$ has poor durability in a 0.5 mol L^{-1} H_2SO_4 solution and is not suitable for long-term use in an acidic medium. The reasons for the sharp decline in the catalytic activity of $Co/Co_3O_4/Ti_3C_2T_x$ in an acidic electrolyte may be as follows: Co and Co_3O_4 were easily dissolved in strong acids. The stability test shows that the $Co/Co_3O_4/Ti_3C_2T_x$ catalyst is not suitable for long-term use in an acidic medium.

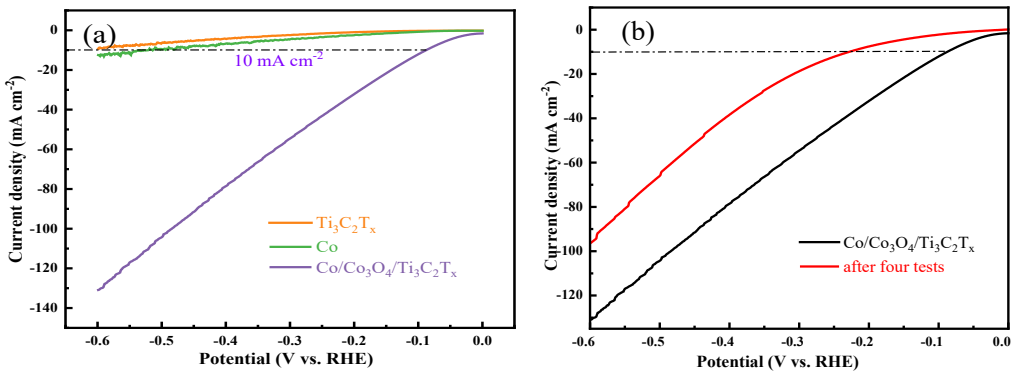


Figure 10. LSV diagram of (**a**) $Ti_3C_2T_x$, Co and $Co/Co_3O_4/Ti_3C_2T_x$; (**b**) $Co/Co_3O_4/Ti_3C_2T_x$ (stability test) in 0.5 mol L^{-1} H_2SO_4 electrolyte.

3.3. Electrocatalytic HER Performance Test in Alkaline Electrolyte

The HER performances of $Ti_3C_2T_x$, Co and $Co/Co_3O_4/Ti_3C_2T_x$ were tested in a 1 mol L^{-1} KOH solution, and the obtained LSV results are shown in Figure 11a. The η values corresponding to the above catalysts at a current density of 10 mA cm^{-2} were obtained: $Co/Co_3O_4/Ti_3C_2T_x$ has a smaller η value (87 mV) than Co (443 mV) and $Ti_3C_2T_x$ (541 mV). Thus, the trend of catalytic activity was $Co/Co_3O_4/Ti_3C_2T_x$ > Co > $Ti_3C_2T_x$. In 1 mol L^{-1} KOH, both Co and $Ti_3C_2T_x$ require large η values to perform the HER, which indicates that both Co and $Ti_3C_2T_x$ have poor HER activity. The CV test results of $Ti_3C_2T_x$, Co and $Co/Co_3O_4/Ti_3C_2T_x$ under different scanning rates (10, 20, 30, 40, 50, 60, 70, 80, 90 and 100 mV s^{-1}) are shown in Figure 11b–d. Based on the CV test results of each catalyst, their C_{dl} values were obtained according to Equation (2). The C_{dl} values of $Ti_3C_2T_x$, Co and $Co/Co_3O_4/Ti_3C_2T_x$ were 9.86 mF cm^{-2}, 7.59 mF cm^{-2} and 28.34 mF cm^{-2}, respectively (see Figure 11e). According to Equation (3), the C_{dl} value can be converted to the ECSA value, and the ECSA values of $Ti_3C_2T_x$, Co and $Co/Co_3O_4/Ti_3C_2T_x$ were 246.50 cm^2 189.75 cm^2 and 708.5 cm^2, respectively. It can be seen that $Co/Co_3O_4/Ti_3C_2T_x$ has the largest electrochemically active area. The Tafel slope values of $Ti_3C_2T_x$, Co and $Co/Co_3O_4/Ti_3C_2T_x$ in a 1 mol L^{-1} KOH electrolyte were calculated according to Equation (4). The Tafel slope value of $Co/Co_3O_4/Ti_3C_2T_x$ was 61.90 mV dec^{-1}, which is better than the 263.09 mV dec^{-1} of Co and 324.46 mV dec^{-1} of $Ti_3C_2T_x$ (seen Figure 11f). The smaller Tafel slope value indicates that the $Co/Co_3O_4/Ti_3C_2T_x$ catalyst has a fast kinetic process in a 1 mol L^{-1} KOH solution. Meanwhile, the Tafel slope values indicate that the $Co/Co_3O_4/Ti_3C_2T_x$ catalyst follows the Volmer–Heyrovsky mechanism. Co/Co_3O_4 can accelerate the adsorption and deionization of H_2O to synthesize H_2. When water molecules are adsorbed on the Co/Co_3O_4 interface, the Co_3O_4 phase helps to split the HO-H bond and produce adsorbed hydroxide ions (OH^-) and hydrogen atoms (H_{ads}), while the Co phase can integrate H_{ads} to produce H_2 [29].

The long-term durability of the $Co/Co_3O_4/Ti_3C_2T_x$ catalyst was tested in a 1 mol L^{-1} KOH electrolyte, and the LSV results are shown in Figure 11g. Compared with the initial curve, the LSV curve did not change significantly after 1000 CV cycles, and the η value was only 8 mV different, indicating that $Co/Co_3O_4/Ti_3C_2T_x$ had good cyclic stability in a 1 mol L^{-1} KOH electrolyte. In addition, in order to better reflect the activity changes of $Co/Co_3O_4/Ti_3C_2T_x$ before and after 1000 CV tests, the MA value of $Co/Co_3O_4/Ti_3C_2T_x$ before and after 1000 CV cycles was calculated from Equation (5). Before the stability test, the MA value of $Co/Co_3O_4/Ti_3C_2T_x$ was 67.57 mA $(mgCo)^{-1}$. After the stability test, the MA value of $Co/Co_3O_4/Ti_3C_2T_x$ was 60.14 mA $(mgCo)^{-1}$. The MA value of $Co/Ti_3C_2T_x$ did not change much after 1000 CV cycles, and the activity of $Co/Co_3O_4/Ti_3C_2T_x$ could still be maintained at 89% after 1000 CV cycles. The results show that $Co/Co_3O_4/Ti_3C_2T_x$ has good catalytic stability in a 1 mol L^{-1} KOH solution.

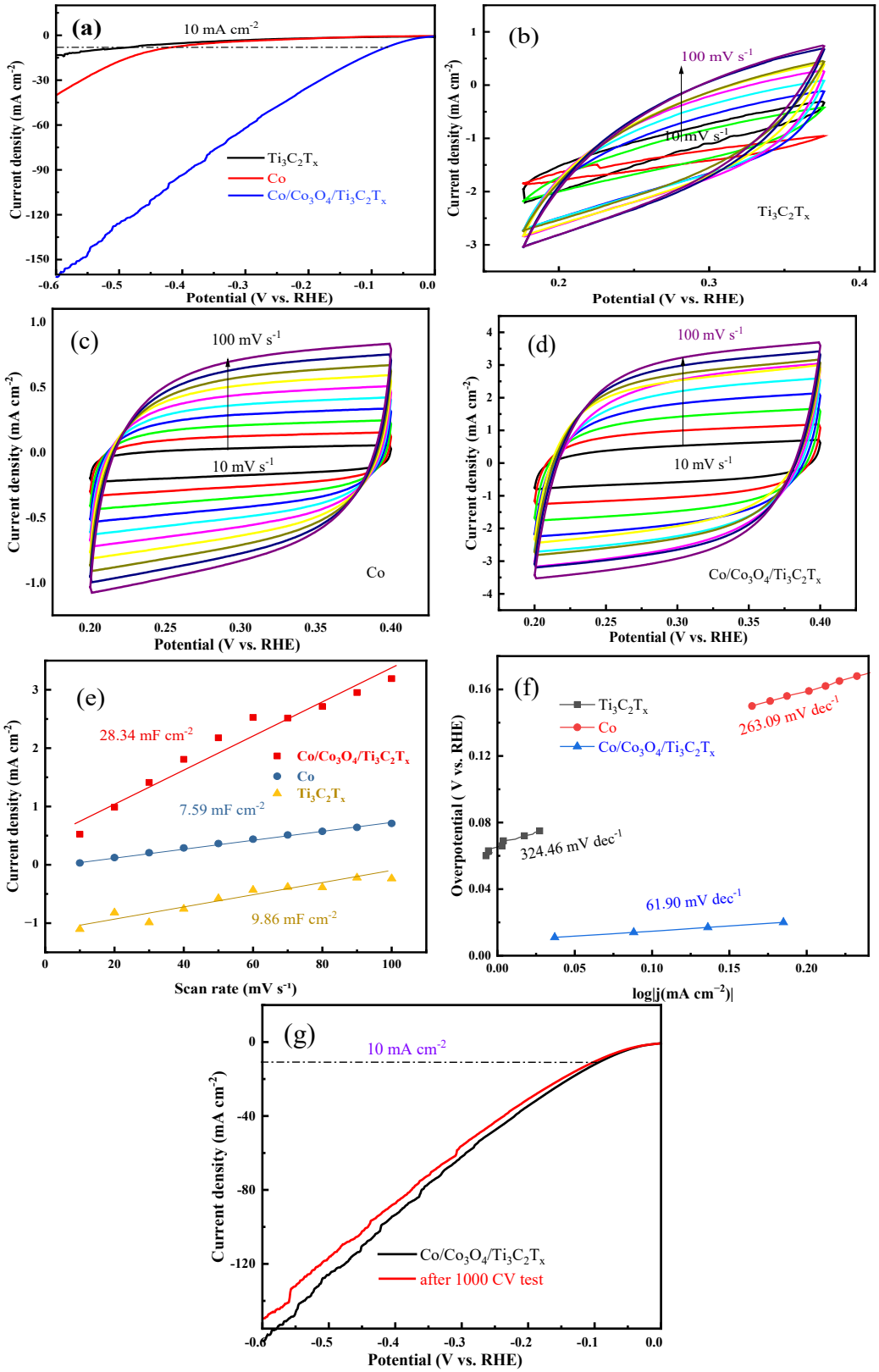


Figure 11. (**a**): LSV diagram of $Ti_3C_2T_x$, Co and $Co/Co_3O_4/Ti_3C_2T_x$ in 1 mol L^{-1} KOH electrolyte; CV results of (**b**) $Ti_3C_2T_x$, (**c**) Co and (**d**) $Co/Co_3O_4/Ti_3C_2T_x$ under different scanning rates (10, 20, 30, 40, 50, 60, 70, 80, 90 and 100 mV s^{-1}); (**e**) C_{dl} value and (**f**) Tafel diagram of $Ti_3C_2T_x$, Co and $Co/Co_3O_4/Ti_3C_2T_x$; (**g**) LSV diagram of $Co/Co_3O_4/Ti_3C_2T_x$ (stability test) in 1 mol L^{-1} KOH electrolyte.

The electrocatalytic performance for the HER of the synthesized $Co/Co_3O_4/Ti_3C_2T_x$ was compared with that of MXene-based catalysts reported in the literature, and the results are shown in Table 2. It could be seen from the table that the $PtCo/Ti_3C_2T_x$ catalyst prepared in this study had better performance in terms of its overpotential and Tafel slope, making it a promising electrocatalyst for the HER.

Table 2. Comparison of electrocatalytic performances for HERs of representative MXene-based catalysts.

Type of Electrocatalyst	Electrolyte	Electrochemical Performance	Refs.
$COF/Ti_3C_2T_x$	0.5 M H_2SO_4	A very low onset potential of 19 mV and a small Tafel slope of 50 mV dec^{-1}	[30]
$MIL/Ti_3C_2T_x$	0.5 M H_2SO_4	An operating overpotential of 107 mV at 10 mA/cm^2	[31]
Mo_2CT_x	0.5 M H_2SO_4	A low overpotential of 283 mV at 10 mA cm^{-2} and an average TOF of −0.02 H_2 s^{-1} at 200 mV	[32]
$MoS_2/Ti_3C_2/C$	0.5 M H_2SO_4	A low overpotential of 135 mV at 10 mA cm^{-2} and a Tafel slope of 45 mV dec^{-1}	[33]
$Co\text{-}MoS_2/Mo_2CT_x$	1 M KOH	A low overpotential of 112 mV at 10 mA cm^{-2} and a Tafel slope of 82 mV dec^{-1}	[34]
$Co/Co_3O_4/Ti_3C_2T_x$	1 M KOH	A low overpotential of 87 mV at 10 mA cm^{-2} and a Tafel slope of 105.17 mV dec^{-1}	This work

4. Conclusions

In this study, the $Co/Co_3O_4/Ti_3C_2T_x$ catalyst was synthesized by supporting Co/Co_3O_4 with $Ti_3C_2T_x$. In a 1 mol L^{-1} KOH solution, the $Co/Co_3O_4/Ti_3C_2T_x$ catalyst showed excellent HER performance, with a low overpotential of 87 mV at 10 mA cm^{-2} and a Tafel slope of 105.17 mV dec^{-1}. The smaller Tafel slope value indicates that the $Co/Co_3O_4/Ti_3C_2T_x$ catalyst has a fast kinetic process and follows the Volmer–Heyrovsky mechanism in a 1 mol L^{-1} KOH solution. The results also show that $Co/Co_3O_4/Ti_3C_2T_x$ has good catalytic stability in a 1 mol L^{-1} KOH solution, and the activity of $Co/Co_3O_4/Ti_3C_2T_x$ could still be maintained at 89% after 1000 CV cycles. It can be expected that these results provide a possible new way to design and prepare a low-cost, high-performance HER catalyst.

Author Contributions: Conceptualization, B.W. and Q.S.; methodology, B.W. and W.G.; validation, W.G., B.W. and Q.S.; formal analysis, Q.S.; investigation, B.W.; resources, Q.S.; data curation, B.W. and W.G.; writing—original draft preparation, B.W. and W.G.; writing—review and editing, Q.S.; supervision, Q.S.; project administration, Q.S.; funding acquisition, Q.S. All authors have read and agreed to the published version of the manuscript.

Funding: This research received no external funding.

Data Availability Statement: The original contributions presented in the study are included in the article, further inquiries can be directed to the corresponding author.

Conflicts of Interest: The authors declare no conflict of interest.

References

1. Song, H.; Luo, S.; Huang, H.; Deng, B.; Ye, J. Solar-driven hydrogen production: Recent advances, challenges, and future perspectives. *ACS. Energy. Lett.* **2022**, *7*, 1043–1065. [CrossRef]
2. Cheng, R.; Min, Y.; Li, H.; Fu, C. Electronic structure regulation in the design of low-cost efficient electrocatalysts: From theory to applications. *Nano Energy* **2023**, *115*, 108718. [CrossRef]
3. Yusuf, B.A.; Yaseen, W.; Xie, M.; Zayyan, R.S.; Muhammad, A.I.; Nankya, R.; Xie, J.; Xu, Y. Recent advances in understanding and design of efficient hydrogen evolution electrocatalysts for water splitting: A comprehensive review. *Adv. Colloid Int. Sci.* **2023**, *311*, 102811. [CrossRef] [PubMed]
4. Zhao, L.; Wu, R.; Wang, J.; Li, Z.; Wei, X.; Chen, J.S.; Chen, Y. Synthesis of noble metal-based intermetallic electrocatalysts by space-confined pyrolysis: Recent progress and future perspective. *J. Energy Chem.* **2021**, *60*, 61–74. [CrossRef]
5. Wu, H.; Alkhatami, A.G.; Farhan, Z.A.; AbdalSalam, A.G.; Hamadan, R.; Aldarrji, M.Q.; Izzat, S.E.; Yosif, A.A.; Hadrawi, S.K.; Riyahi, Y.; et al. Recent developments in the production of hydrogen: Efficiency comparison of different techniques, economic dimensions, challenges and environmental impacts. *Fuel Process. Technol.* **2023**, *248*, 107819. [CrossRef]

6. Wang, Y.; Yan, D.; Hankari, S.E.; Zou, Y.; Wang, S. Recent progress on layered double hydroxides and their derivatives for electrocatalytic water splitting. *Adv. Sci.* **2018**, *5*, 1800064. [CrossRef] [PubMed]
7. Wang, C.; Li, Y.; Gu, C.; Zhang, L.; Wang, X.; Tu, J. Active Co@CoO core/shell nanowire arrays as efficient electrocatalysts for hydrogen evolution reaction. *Chem. Eng. J.* **2022**, *429*, 132226. [CrossRef]
8. Liu, H.; He, P.; Wang, S.; Gao, J.; Zhou, L.; Li, C.; Zhang, Y.; Yang, D.; He, M.; Jia, L.; et al. Facile one-step fabrication of bimetallic Co–Ni–P hollow nanospheres anchored on reduced graphene oxide as highly efficient electrocatalyst for hydrogen evolution reaction. *Int. J. Hydrogen. Energy* **2019**, *44*, 24140–24150. [CrossRef]
9. Li, T.; Niu, K.; Yang, M.; Shrestha, N.K.; Gao, Z.; Song, Y. Ultrathin CoS_2 shells anchored on Co_3O_4 nanoneedles for efficient hydrogen evolution electrocatalysis. *J. Power Sources* **2017**, *356*, 89–96. [CrossRef]
10. Zhang, X.; Bi, Y.; Wang, Y.; Liu, Q.; Zhang, Y.; Wang, J.; Chen, L. S co-doped graphene coupled with Ni_2P/CoP-loaded carbon nanospheres: A novel catalyst for hydrogen evolution reaction. *Mater. Today Sustain.* **2024**, *25*, 100677. [CrossRef]
11. Lin, B.; Chen, J.; Yang, R.; Mao, S.; Qin, M.; Wang, Y. Multi-hierarchical cobalt-based electrocatalyst towards high rate H_2 production. *Appl. Catal. B Environ.* **2022**, *316*, 121666. [CrossRef]
12. Hanan, A.; Lakhan, M.N.; Bibi, F.; Khan, A.; Soomro, I.A.; Hussain, A.; Aftab, U. MOFs coupled transition metals, graphene, and MXenes: Emerging electrocatalysts for hydrogen evolution reaction. *Chem. Eng. J.* **2024**, *482*, 148776. [CrossRef]
13. Ali, S.A.; Sadiq, I.; Ahmad, T. Superlative porous organic polymers for photochemical and electrochemical CO_2 reduction applications: From synthesis to functionality. *Langmuir* **2024**, *40*, 10414–10432. [CrossRef] [PubMed]
14. Ali, S.A.; Ahmad, T. MBenes for energy conversion: Advances, bottlenecks, and prospects. *Langmuir* **2024**, *40*, 10835–10846. [CrossRef]
15. Karthikeyan, S.C.; Sidra, S.; Ramakrishnan, S.; Kim, D.H.; Sagayaraj, P.J.; Sekar, K.; Yoo, D.J. Heterostructured NiO/IrO_2 synergistic pair as durable trifunctional electrocatalysts towards water splitting and rechargeable zinc-air batteries: An experimental and theoretical study. *Appl. Catal. B Environ. Energy* **2024**, *355*, 124196. [CrossRef]
16. Shaikh, Z.A.; Laghari, A.A.; Litvishko, O.; Litvishko, V.; Kalmykova, T.; Meynkhard, A. Liquid-phase deposition synthesis of ZIF-67-derived synthesis of Co_3O_4@TiO_2 composite for efficient electrochemical water splitting. *Metals* **2021**, *11*, 420. [CrossRef]
17. Sheng, H.; Ye, K.; Gao, Y.; Zhu, K.; Yan, J.; Wang, G.; Cao, D. Simultaneously boosting hydrogen production and ethanol upgrading using a highly-efficient hollow needle-like copper cobalt sulfide as a bifunctional electrocatalyst. *J. Colloid Interface Sci.* **2021**, *602*, 325–333. [CrossRef] [PubMed]
18. Yang, Z.; Liu, A.; Wang, C.; Liu, F.; He, J.; Li, S.; Wang, J.; You, R.; Yan, X.; Sun, P.; et al. Improvement of gas and humidity sensing properties of organ-like MXene by alkaline treatment. *ACS Sens.* **2019**, *4*, 1261–1269. [CrossRef] [PubMed]
19. Liu, S.; Deng, T.; Hu, X.; Shi, X.; Wang, H.; Qin, T.; Zhang, X.; Qi, J.; Zhang, W.; Zheng, W. Increasing surface active Co^{2+} sites of MOF-derived Co_3O_4 for enhanced supercapacitive performance via $NaBH_4$ reduction. *Electrochim. Acta* **2018**, *289*, 319–323. [CrossRef]
20. Cao, S.; Shen, B.; Tong, T.; Fu, J. 2D/2D heterojunction of ultrathin MXene/Bi_2WO_6 nanosheets for improved photocatalytic CO_2 reduction. *Adv. Funct. Mater.* **2018**, *28*, 1800136. [CrossRef]
21. Feng, A.; Yu, Y.; Wang, F.; Jiang, Y.; Yu, L.; Mi, L.; Song, L. Two-dimensional MXene Ti_3C_2 produced by exfoliation of Ti_3AlC_2. *Mater. Design.* **2017**, *114*, 161–166. [CrossRef]
22. Ma, Y.Y.; Lang, Z.L.; Yan, L.K.; Wang, Y.H.; Tan, H.Q.; Feng, K.; Xia, Y.J.; Zhong, J.; Liu, Y.; Kang, Z.H.; et al. Highly efficient hydrogen evolution triggered by a multi-interfacial Ni/WC hybrid electrocatalyst. *Energy Environ. Sci.* **2018**, *11*, 2114–2123. [CrossRef]
23. Eid, K.; Lu, Q.; Abdel-Azeim, S.; Soliman, A.; Abdullah, A.M.; Abdelgwad, A.M.; Forbes, R.P.; Ozoemena, K.I.; Varma, R.S.; Shibl, M.F. Highly exfoliated $Ti_3C_2T_x$ MXene nanosheets atomically doped with Cu for efficient electrochemical CO_2 reduction: An experimental and theoretical study. *J. Mater. Chem. A* **2022**, *10*, 1965–1975. [CrossRef]
24. Islam, M.M.; Faisal, S.N.; Akhter, T.; Roy, A.K.; Minett, A.I.; Konstantinov, K.; Shi, X.D. Liquid-crystal-mediated 3D macrostructured composite of Co/Co_3O_4 embedded in graphene: Free-standing electrode for efficient water splitting. *Part. Part. Syst. Character.* **2017**, *34*, 1600386. [CrossRef]
25. Ding, D.; Shen, K.; Chen, X.; Chen, H.; Chen, J.; Fan, T.; Wu, R.; Li, Y. Multi-level architecture optimization of MOF-templated Co-based nanoparticles embedded in hollow N-doped carbon polyhedra for efficient OER and ORR. *ACS Catal.* **2018**, *8*, 7879–7888. [CrossRef]
26. McCrum, I.T.; Koper, M.T.M. The role of adsorbed hydroxide in hydrogen evolution reaction kinetics on modified platinum. *Nat. Energy* **2020**, *5*, 891–899. [CrossRef]
27. Wu, J.; Fan, J.; Zhao, Y.; Wang, D.; Wang, H.; Liu, L.; Gu, Q.; Zhang, L.; Zheng, X.; Cui, D.J.; et al. Atomically dispersed MoO_x on rhodium metallene boosts electrocatalyzed alkaline hydrogen evolution. *Angew. Chem. Int. Edit.* **2022**, *61*, 202207512.
28. Do, H.H.; Tekalgne, M.A.; Tran, V.A.; Le, Q.V.; Cho, J.H.; Ahn, S.H.; Kim, S.Y. MOF-derived Co/Co_3O_4/C hollow structural composite as an efficient electrocatalyst for hydrogen evolution reaction. *Fuel* **2022**, *329*, 125468. [CrossRef]
29. Iqbal, M.F.; Gao, W.; Mao, Z.; Hu, E.; Gao, X.; Zhang, J.; Chen, Z. Strategies to enhance the electrocatalytic behavior of metal selenides for hydrogen evolution reaction: A review. *Int. J. Hydrogen. Energy* **2023**, *48*, 36722–36749. [CrossRef]
30. Ma, C.; He, H.; Qin, J.; Luo, L.; Lan, Y.; Zhang, J.; Yang, L.; Jiang, Q.; Huang, H. The marriage of hydrazone-linked covalent organic frameworks and MXene enables efficient electrocatalytic hydrogen evolution. *Small Struct.* **2024**, *5*, 2300279. [CrossRef]

31. Ma, C.; He, H.; Qin, J.; Hao, L.; Jia, L.; Yang, L.; Huang, H. Combining MXene nanosheets with iron-based metal-organic frameworks for enhanced electrocatalytic hydrogen evolution reaction. *Mater. Today Chem.* **2023**, *30*, 101531. [CrossRef]
32. Seh, Z.W.; Fredrickson, K.D.; Anasori, B.; Kibsgaard, J.; Strickler, A.L.; Lukatskaya, M.R.; Gogotsi, Y.; Jaramillo, T.F.; Vojvodic, A. Two-dimensional molybdenum carbide (MXene) as an efficient electrocatalyst for hydrogen evolution. *ACS Energy Lett.* **2016**, *1*, 589–594. [CrossRef]
33. Wu, X.; Wang, Z.; Yu, M.; Xiu, L.; Qiu, J. Stabilizing the MXenes by carbon nanoplating for developing hierarchical nanohybrids with efficient lithium storage and hydrogen evolution capability. *Adv. Mater.* **2017**, *29*, 1607017. [CrossRef] [PubMed]
34. Liang, J.; Ding, C.; Liu, J.; Chen, T.; Peng, W.; Li, Y.; Zhang, F.; Fan, X. Heterostructure engineering of Co-doped MoS_2 coupled with Mo_2CT_x MXene for enhanced hydrogen evolution in alkaline media. *Nanoscale* **2019**, *11*, 10992–11000. [CrossRef] [PubMed]

Disclaimer/Publisher's Note: The statements, opinions and data contained in all publications are solely those of the individual author(s) and contributor(s) and not of MDPI and/or the editor(s). MDPI and/or the editor(s) disclaim responsibility for any injury to people or property resulting from any ideas, methods, instructions or products referred to in the content.